Kinetic modeling and experiments of pulsed response of two noble gas plasma

IEPC-2022-587

Presented at the 37th International Electric Propulsion Conference
Massachusetts Institute of Technology, Cambridge, MA, USA
June 19-23, 2022

Toyofumi Yamauchi[1], Nakul Nuwal[2], Joshua L. Rovey[3], and Deborah A. Levin[4]
The University of Illinois at Urbana-Champaign, Urbana, IL, 61801, the United States

This paper presents the preliminary results of the experimental activities to improve our understanding of molecular-based multi-species plasmas and to develop electric propulsion plasma thrusters using these gases as propellants. The formation and propagation of ion acoustic waves in a low-density plasma generated in a multipole plasma cell with a hot filament discharge were studied to understand the dynamic behaviors and the sheath/presheath conditions of the low-density multi-species plasma. The electron temperature of the low-density (on the order of 10^{13} m^{-3}) argon plasma was determined by a disk-shaped Langmuir probe. The ion acoustic wave was formed by a fast pulsed voltage applied on a mesh-grid electrode immersed in the plasma. A phase speed of the formed ion acoustic wave was determined by spatial measurements of the response of the plasma perturbed by the applied pulse. In this experiment, the shape of the pulse applied to the wave launcher, a biasing voltage on the wave collector, and a background chamber pressure were varied to validate the experimental setup. The electron temperature determined by the measured phase speed of ion acoustic wave ($v_{IAW} = \sqrt{eT_e/m_i}$) agreed with the electron temperature obtained by the Langmuir probe with a 40 % error maximum.

I. Nomenclature

A_c	=	effective ion collection area
A_p	=	probe area
b	=	impact parameter
B_{center}	=	magnetic field strength at center of MPC
$B_{\text{near-wall}}$	=	magnetic field strength near MPC wall
e	=	elementary charge
I_{dis}	=	discharge current
I_e	=	electron-only current
I_i	=	ion-only current
I_{measured}	=	measured current
I_{LmP}	=	IIEE-adjusted current
k	=	wavenumber
k_B	=	Boltzmann constant
K_eff	=	effective rate constant
m_x	=	mass of ion x
m_i	=	ion mass

[1]Graduate Research Assistant, Department of Aerospace Engineering, ty20@illinois.edu
[2]Graduate Research Assistant, Department of Aerospace Engineering, nuwal2@illinois.edu
[3]Associate Professor, Department of Aerospace Engineering
[4]Professor, Department of Aerospace Engineering

n_x = density of neutral x
n_{x^+} = density of ion x
n_e = electron density
$n_{e,s}$ = electron density at sheath edge
P_{chamber} = chamber background pressure
r_{LmP} = radius of Langmuir probe
T_e = electron temperature
T_i = ion temperature
$T_{i,s}$ = ion temperature at sheath edge
v_B = Bohm speed
$v_{i,s}$ = ion speed at sheath edge
V_{bat} = 45-V biasing battery unit voltage
V_p = plasma potential
Z_{LC} = distance between wave launcher and wave collector
α = factor of density drop in presheath
λ_D = Debye length
Φ_{ps} = potential drop in presheath
σ_{iz} = ionization cross-section
γ = IIEE yield

II. Introduction

Electric propulsion (EP) is a technology that utilizes electrical power to accelerate a propellant for gaining a thrust. EP has been researched and developed over a half-decade and has provided a large delta-V in space to many spacecrafts, significantly reducing launch costs, extending mission lifetimes, and making deep-space exploration missions possible. EP often uses electrical power to ionize a propellant to convert electrical energy into kinetic energy via the generated plasma. Traditional EP plasma thrusters have utilized a noble gas, especially xenon, for their propellant because 1) it is relatively easy to be ionized, 2) it is not chemically reactive with materials used in spacecraft and does not cause a contamination problem, and 3) it is not toxic and safe to human. Recently, EP plasma thrusters using alternative propellants, i.e., molecular-based gas, are getting much attention from industrial and military fields. The use of molecular-based gas as propellant is beneficial in several ways, such as eliminating a high-pressure gas tank, saving a cost for expensive noble gas, and potential in-situ refueling at deep-space destinations. Utilizing molecular-based gas is an important technical milestone for advanced EP plasma thrusters.

Multimode propulsion (MP) integrates two or more propulsive modes into a single propulsion system with a shared propellant [1–3]. Mass saving achieved by propellant sharing is a foremost benefit of MP. Furthermore, a combination of high-efficiency, low-thrust EP and low-efficiency, high-thrust chemical propulsion (CP) offers a mission designer more trajectory options and flexibilities, and it may become an essential technology for a particular space mission. However, in terms of shared propellants, conventional EP propellants (i.e., noble gas) are unsuitable for MP because CP typically utilizes chemical reactions (i.e., combustion) to gain a high thrust. In contrast, plasmas of chemically reacting gas, such as O_2, N_2, CO_2, H_2O, and NH_3, have been widely used in a plasma processing field, and these molecular-based gases can be reasonable candidates for MP propellant. Air-breathing electric propulsion (ABEP) is the utilization of EP for very-low Earth orbit (VLEO, <500 km altitude) operation [4–8]. At the VLEO, the ambient air is too thin for traditional aerodynamic control and air-breathing propulsion but too thick for continuous drag compensation with low-efficiency CP engines. In principle, the ABEP collects air in front of the spacecraft and accelerates it to gain a continuous low thrust that compensates for the weak drag force acting on it. However, the fraction of the noble gas in the air is tiny (<1%) at any altitudes, and conventional EP thrusters using xenon may not perform well with the collected air without design modifications and optimizations. Therefore, the propellant used in ABEP thrusters would be the air (a mixture of N_2, O_2, O, N, and Ar). These two are the specific applications of the utilization of molecular-based gas in EP plasma thrusters, and numberless works to realize these thrusters have been conducted numerically and experimentally.

However, some challenges still exist with these new EP plasma thrusters using molecular-based gas propellants. Experimental performance measurements revealed that the performance of EP plasma thrusters using molecular-based gas propellants was inferior to that of thrusters using xenon. Several studies have concluded that these are mainly due to the low mass utilization (i.e., ionization) efficiency of molecular-based gases [9–14]. One approach to resolve this issue is reducing the generated plasma loss. In EP plasma thrusters, the main plasma loss mechanism is the loss at the

boundary via a sheath. The lack of understanding of the sheath physics of molecular-based multi-species plasma, such as ion's behavior at the sheath boundary, makes it challenging to apply conventional plasma diagnostic methods, such as electrostatic probes, to such a more complex plasma. It is one of the reasons that previous experimental works have focused on concept validation and performance measurements, and in-thruster plasma physics was rarely investigated. Even in a single-species noble gas plasma, the sheath physics of a low-density plasma is not fully understood yet. As mentioned above, the mass utilization efficiency of molecular-based gas is low, and it may force us to design the EP plasma thruster operating with a low-density plasma. However, not many studies have been carried out for low-density plasma because the plasma industry, such as semiconductor processing, prefers high-density plasma for a faster production rate and more precise manufacturing ability. Optical diagnostic methods, such as LIF (laser-induced fluorescence), are powerful tools for multi-species plasmas, and their non-invasive nature is quite attractive, especially for small EP thrusters. However, since these techniques rely on the spectrum emission from the plasma, they often cannot be used for low-density plasmas. On the other hand, even at a low-density level, electrostatic probes collecting charged particles via a sheath formed around them can detect electrical signals with a reasonable signal-to-noise ratio. Therefore, understanding the plasma physics, especially on sheath in this study, of the molecular-based multi-species plasma and the low-density plasma will improve a measurement technique for future EP plasma thrusters using molecular-based alternative propellants, and it will potentially increase the performances of these thrusters by optimizing the thruster design with an advanced understanding of the plasma loss mechanism via the sheath. Due to a large length-scale (i.e., the Debye length) and slow timescale (i.e., plasma frequency) of low-density plasma, the empirical design parameters built up for years in the EP community may not be appropriate for new EP plasma thruster operating at low-density plasma. Understanding the low-density plasma physics is essential for us to expand the boundary of EP technologies, which may find a particular niche.

This paper studies the formation and propagation of an ion acoustic wave (IAW) in a low-density single-species argon plasma as a foundation of molecular-based multi-species plasma research. IAW is one type of longitudinal oscillation of ions and electrons in plasma similar to sound waves in air [15]. Studying the IAW as a dynamic plasma phenomenon is important because EP plasma thrusters are dynamic plasma devices, and the capability of time-resolved measurements is essential for EP plasma thruster development. The IAW can be excited by applying the fast pulsed voltage to the electrode immersed in the plasma. Therefore, the formation of the IAW is closely related to a sheath formation mechanism, and the characterization of the IAW may give us insights into the sheath/presheath conditions in the plasma. In the limit of cold-ion ($T_e \gg T_i$) and the limit of the large product of wave number and Debye length ($k\lambda_D \gg 1$), the phase speed of IAW is given by [15, 16]

$$v_{\mathrm{IAW}} = \frac{\omega}{k} = \sqrt{\frac{eT_e}{m_i}} = v_B \tag{1}$$

This speed is also known as a Bohm speed. In such limits, and when the plasma is single-species, the plasma's electron temperature can be determined by measuring the phase speed of the IAW. The electron temperature determined by the phase speed of the IAW is compared to the ones obtained by a Langmuir probe measurement.

The single-species argon plasma is generated in the multipole plasma cell (MPC) with a hot filament discharge. Previously, several researchers have established the method to characterize a plasma in the MPC using the IAW [17–20]. This method has been expanded to a noble-gas multi-species plasma to determine the relative ion concentration [17, 21]. When there are two types (i.e., two-species) of ions are present in the plasma, the speed of the IAW is given by [21]

$$v_{\mathrm{IAW}} = \sqrt{\frac{n_{1^+}}{n_e}\frac{T_e}{m_1} + \frac{n_{2^+}}{n_e}\frac{T_e}{m_2}} \tag{2}$$

When the electron temperature and two ion species are known, the relative ion concentration can be determined using Eq. 2. For example, the ion species 1 density relative to the electron density is given by

$$\frac{n_{1^+}}{n_e} = \frac{v_{IAW}^2 - v_{B,2}^2}{v_{B,1}^2 - v_{B,2}^2} \tag{3}$$

Equations 2 and 3 are true only for a quasi-neutral plasma having only positively-charged ions, which can be expressed as

$$n_e = n_{1^+} + n_{2^+} + \ldots = \sum n_{i^+} \tag{4}$$

To the best of our knowledge, such techniques have been applied only to a medium-density ($n_e > 10^{15}$ m^{-3}) noble-gas single-species plasma.

III. Experimental Setup

Figure 1 shows our plasma discharge and diagnostic setups.

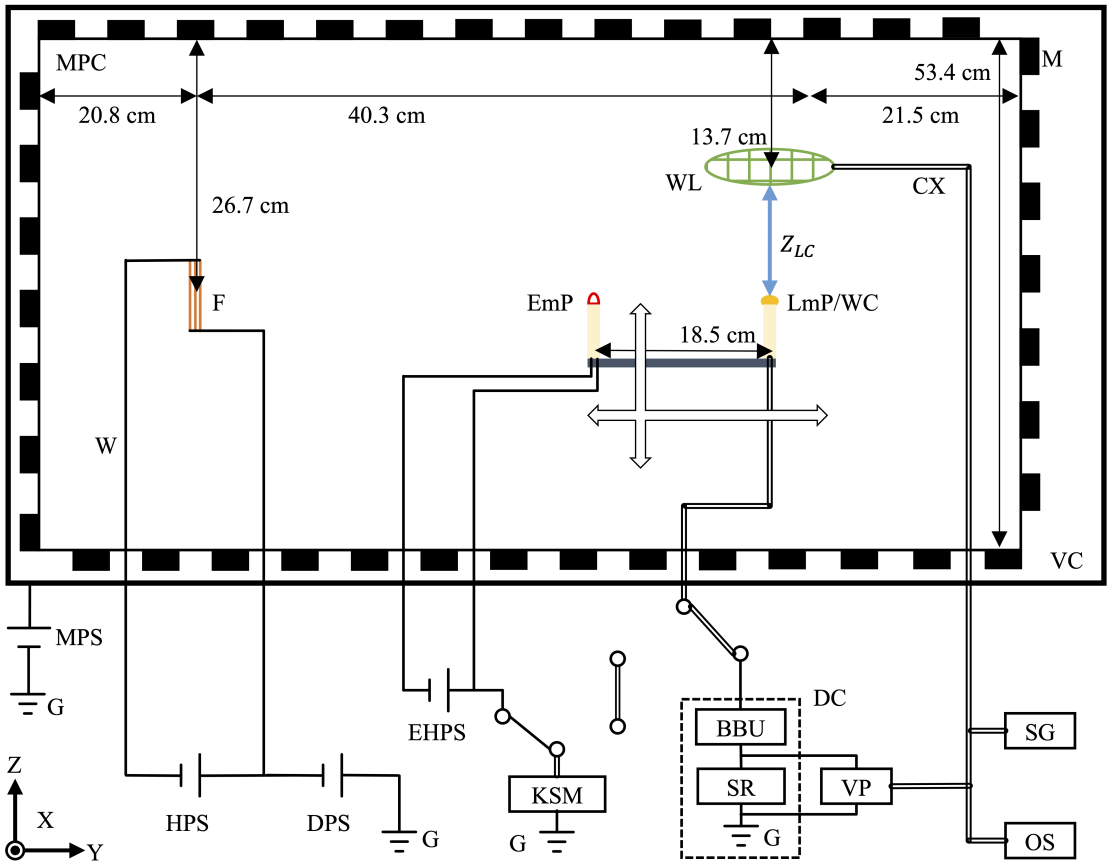

Fig. 1 Experimental Setup: BBU = 45-V Biasing Battery Unit, CX = Coaxial Cable, DC = Detection Circuit, DPS = Discharge Power Supply, EHPS = Heating Power Supply for EmP, EmP = Emissive Probe, F = Filaments, G = Ground, HPS = Heating Power Supply, KSM = Keithley Source Meter, LmP = Langmuir Probe, M = Magnets, MPC = Multipole Plasma Cell, MPS = MPC biasing PS, OS = Oscilloscope, SG = Signal Generator, SR = Sensing Resistor, VC = Vacuum Chamber, VP = Voltage Probe, W = Wire, WC = Wave Collector, WL = Wave Launcher, XYZ = the coordinate system (the x-axis coming from the page)

A. Vacuum Facilities

All single-species experiments were conducted in the University of Illinois at Urbana-Champaign Electric Propulsion Test Facility 2 - White Vacuum Chamber. This facility is 1.2 m in diameter and 2.1 m long and evacuated to the chamber base pressure of 5×10^{-8} Torr by a 1.2 m diameter PHPK TM1200 cryopump. The chamber is electrically grounded to the building ground rod. A gas flow into the chamber was controlled by a combination of a HAM-LET needle valve (H300USSLR1/4M) and an Alicat MCV mass flow controller (MCV-500SCCM-D-DB15-PCV10); the needle valve let the majority of flow and the mass-flow-controller adjusted the total flow rate depending on the chamber pressure using the LabVIEW feedback system. P_{chamber} was monitored by a KJLC Cold Cathode Pirani Gauge (KJLC CCPG-H2-6) from atmospheric pressure to the base pressure. In the single-species experiments, an Airgas UHP300 argon with 99.999% purity was used. The chamber pressure was adjusted to 0.1, 0.5, and 1.0 mTorr. Considering the base pressure of 5×10^{-8} Torr, the gas in the chamber was mostly argon (<0.05% air). At these pressures, electron-neutral (e^--Ar) mean free epaths are 1.28, 0.26, and 0.13 m for a collision cross-section of 2.39×10^{-19} m^2 [22, 23]. These are larger than the dimensions of the probes and the distance between the wave launcher and collector. Therefore, a collisionless plasma is assumed for all single-species experiment conditions.

B. Multipole Plasma Cell (MPC)

The plasma was formed in a Multipole Plasma Cell (MPC). Plasmas in an MPC have been widely used for plasma sheath studies [24–27] and SEE (Secondary Electron Emission) measurements [28, 29] when steady, homogeneous Maxwellian plasmas are required. Our MPC is cylindrical, 53.4 cm in diameter, and 82.6 cm long. The magnetic field reflecting electrons to reduce wall losses of plasma was created by placing CM-0127 ceramic disk magnets on the side surface and the top and bottom bases of our MPC. The magnets were held in-line by aluminum u-channels. In each u-channel, the magnets were oriented with the same polarity, and the opposite polarity was assigned on the adjacent u-channel; this configuration formed a broken line cusp magnetic field [30]. The magnets were equally spaced 1.27 cm apart in each u-channel. A total of 766 magnets were used in our MPC. The magnetic fields near the wall were strong enough ($|B_{\text{near-wall}}| > 0.045$ T) to reflect electrons to the bulk plasma but weak enough ($|B_{\text{center}}| < 10^{-6}$ T) to assume non-magnetized plasma throughout most of the domain in the MPC.

The plasma was formed by a hot filament discharge. Primary electrons (i.e., hot electrons thermionically emitted from an array of thoriated tungsten filaments with a diameter of 0.127 mm) collide with neutral atoms to initiate an ionization process. The filaments were placed on the center line of the MPC, approximately 20.8 cm away from one of the bases. The filaments were parallel to the z-direction shown in Fig. 1. The filaments were heated by an electrical current supplied by a TDK-Lambda GENH30V-25A DC power supply. The filaments were biased negatively with respect to the MPC so that the primary electrons gain energy from the potential difference, and they start moving outward from the center-placed filament with enough energy for the ionization. The filaments were biased by a Kepco BOP 1000M DC power supply. The discharge voltage, the potential between the filament and ground, was held at -60 V for all tested conditions. The discharge current, the current emitted from the filament, was varied by changing the filament heating power. The nominal heating power was 6.5 V and 7.5 A.

Our MPC was electrically biased to adjust the plasma potential. It is because we wanted to avoid the sheath formation around the wave launcher before the pulse application, and the wave launcher's potential was limited by the signal generator that generates a signal between -10 and +10 V. Therefore, the plasma potential of -10 V or +10 V was desired. When the MPC was grounded, the measured plasma potential was -4.2 V at a P_{chamber} of 0.5 mTorr. V_p of -10V was achieved by biasing the MPC by a Simply Done Alkaline AA battery with approximately -1.5 V with respect to the ground for all P_{chamber}'s. V_p of +10 V was achieved by biasing the MPC by a Kepco MSK 125-1M DC power supply with +17.0 V with respect to the ground at P_{chamber} of 0.5 mTorr.

C. Electrostatic Probes

The steady-state plasma parameters were determined by two electrostatic probes; the emissive probe (EmP) and Langmuir Probe (LmP). These electrostatic probes were mounted on Velmex XSlide linear motion stages, allowing them to move in the x-z plane shown in Fig. 1. Both probe measurements were conducted in front of the wave launcher, approximately 40.3 cm away from the filaments. When these probes made their measurements, they were placed approximately 13.0 cm away from the front of the wave launcher. It was on approximately the center line of the cylindrical MPC and was considered the most appropriate location to take a probe measurement to get the MPC plasma characteristics because it is least affected by the MPC's wall sheath and magnetic field. Both probes were always separated by approximately 18.5 cm away to minimize the invasive effect due to their physical existence.

V_p was measured by an EmP. Our EmP was made of a thoriated tungsten wire with a diameter of 0.127 mm, enclosed in a ceramic tubing with a diameter of 4.78 mm. About 10 mm of the tungsten wire was exposed at the tip of the ceramic tubing to make a hairpin shape. The EmP was heated by an Agilent E3634A DC power supply with a nominal heating power of 3.5 V and 2.5 A. A Keithley 2410 Sourcemeter biased the probe from -30 V to +20 V with an increment of 0.2 V, collecting the current through the EmP at each biasing voltage. The average dwelling time at each biasing voltage was about 55 ms, much longer than the electron and ion timescales for all tested conditions. Therefore, it is considered that the EmP collected the equilibrium state current corresponding to each biasing voltage.

n_e and T_e were measured by an LmP. Our LmP was disk-shaped with a diameter of 7.7 mm and a thickness of 0.5 mm, made of 99.95% pure tungsten. The LmP's flat surface was placed parallel to the x-y plane shown in Fig. 1 so that it faces the wave launcher. The Keithley 2410 Sourcemeter biased the LmP from -150 to +50 V with an increment of 0.2 V, collecting the current through the LmP at each biasing voltage. Like the EmP, the average dwelling time was also approximately 55 ms, and it is considered that the LmP collected the equilibrium state current corresponding to each biasing voltage.

The analysis method for the data collected by the electrostatic probes is summarized in Appendix A.

D. Wave Launcher and Collector

In order to generate the IAW in the generated plasma, the pulsed voltage was applied to a wave launcher (WL) immersed in the MPC. Our WL was made of 304 stainless steel mesh, with a diameter of 10 cm and a thickness of 0.01 cm. The mesh spacing size was approximately 40 lines/cm. The flat surface of the WL was placed in the x-y plane, as shown in Fig. 1. The center of the WL was placed approximately 13.0 cm away from the center line of the MPC, which was approximately 13.8 cm away from the wall. The center of the WL was approximately 39.0 cm away from the filament and 21.5 cm away from the base. The WL was connected to a Stanford Research System Model PS350 Signal Generator via an RG-58C/U coaxial cable. The signal generator generated a square pulse wave with a pulse width of 100 μs every 10 ms. In other words, the signal generator generated a square wave of a 10 ms period with a duty cycle of 1% (=100 μs/10 ms). The pulse repetition rate was much longer than the plasma's timescales (approximately 50 ns for electrons and 13.4 μs for argon ions), and therefore it is considered that the plasma returned to the unperturbed equilibrium state after each pulse was applied. The amplitude of the applied signal was 20 V, either from +10 V to -10 V or from -10V to +10 V.

In order to observe the response of the perturbed plasma, a wave collector (WC) was placed in the MPC. In our setup, the WC was the LmP connected to the different devices outside the vacuum system. When it was used as the WC, the WC was connected to our detection circuit via the RG-58C/U coaxial cable. The detection circuit consisted of a 45-V biasing battery unit, a 10-kΩ sensing resistor, and the ground. The 45-V biasing battery unit, made of five Energizer Max 9V Alkaline batteries connected in series, was connected to the WC to select a type of charged particles collected by the WC. When the 45-V biasing battery unit was connected to bias the WC negatively (i.e., the - side was on the WC), it is assumed that most of the electrons were repelled by the WC and vice versa. The 45-V biasing battery unit could be taken off from the detection circuit. A current through the WC was obtained by a voltage drop across a 10-kΩ sensing resistor using a Tektronix P2221 Voltage Probe. The voltage probe was connected to a Tektronix DPO 2024 Oscilloscope to measure a change in current due to the applied perturbation. The sampling speed and the bandwidth of the oscilloscope are 1 Giga-sample/s and 200 MHz, respectively. The oscilloscope was directly connected to the signal generator via the RG-58C/U coaxial cable to trigger an oscilloscope measurement. The oscilloscope took a measurement when the applied signal passed 0V either in a rising or falling direction. The signal through the detection circuit was recorded from -100 μs to +900 μs from the triggering event. The oscilloscope took an average of the last 128 signals to reduce signal noise. Based on the test without plasma, the detection circuit responds to an applied pulse within 1 μs, which is short enough to observe phenomena with an ion timescale. The WC was mounted on the Velmex XSlide to collect the signal at multiple locations. Z_{LC}, the distance between the WL and the WC, was varied by the linear motion stage from 20 mm to 130 mm.

Figure 2 shows one of the data collected during the wave excitation experiments (when $P_{chamber}$ = 1.0 mTorr, I_{dis} = 30 mA, and the 45-V biasing battery unit was not in the detection circuit (V_{bat} = 0 V)). The signals before 50 μs and after 500 μs are not included in Figs. 2a and 2b. Figure 2a shows the signals applied to the WL vs. time at different Z_{LC}'s. The applied signals were independent of Z_{LC}, and it confirms that the WL applied the same pulsed voltage for different Z_{LC}'s. In Fig. 2b, the signals collected by the WC at different Z_{LC}'s were presented. The coloring rule in Fig. 2b is the same as the one in Fig. 2a. The collected signals were smoothed out using the MATLAB® *smoothdata* function. The '*movmean*' method, which performs a moving-average to a selected window, was selected for the MATLAB® *smoothdata*. The window size was 200 was used here. The collected data before being smoothed ('the raw data') was presented only for Z_{LC} = 20 mm in Fig. 2b for visual representation of smoothing effect. The difference in the collected signal amplitude at an unperturbed domains (before 100 μs and approximately after 370 μs) shown in Fig. 2b increased as Z_{LC} increases. It is considered that it was caused by the plasma number density profile caused by the sheath formed around the WL. After a short time (a few tens of microseconds) of the pulsed voltage application to the WL, the WC collected time-varying signals with a clear peak. That peak was obtained by applying the MATLAB® *min* function on the searching domain between two vertical solid black lines (210 and 300 μs). The obtained peak is represented as a circle in Fig. 2b. Figure 2c shows Z_{LC}'s vs. the arrival time of the first peak for each collected signal at different Z_{LC}. The arrival time is counted with respect to the time when the pulse application ends (here 200 *mu*s). The black dot line represented the linear fitted curve. The slope of the curve represented the phase speed of the generated wave. In this case, the phase velocity is approximately 1630 m/s. Here, it is assumed that there is approximately 10% error in Z_{LC}, and $\pm$20 μs for the arrival time determination. It is approximately a few mm to ten mm for Z_{LC}, and a 5-10% error for the arrival time. Based on the error propagation theory, the estimated error in the phase speed determination is approximately 15%. Therefore, the error size for the phase velocity is approximately a few hundred meter-per-seconds in this case.

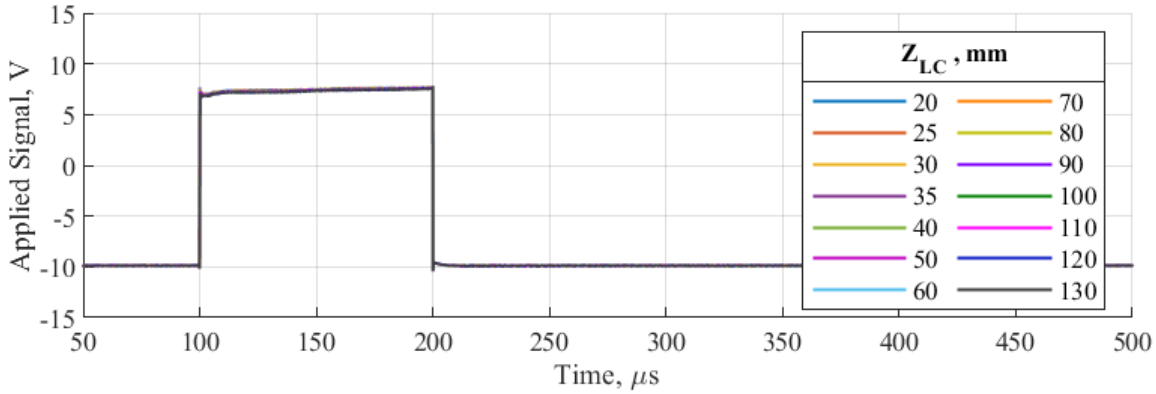

(a) Applied Signals vs. Time

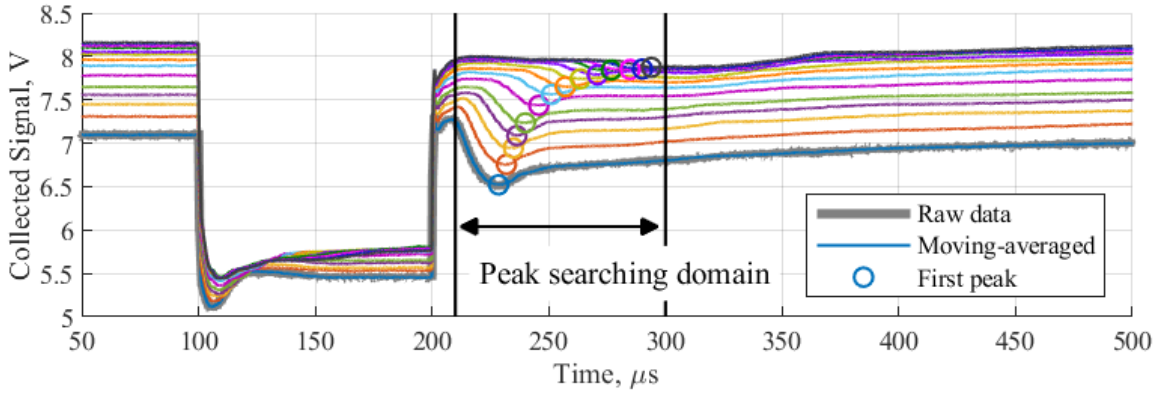

(b) Collected Signals vs. Time (The coloring rule is the same as the ones in Fig. 2a)

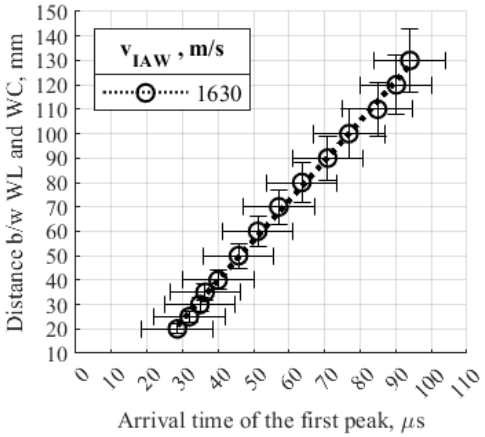

(c) Distance between WL and WC vs. Arrival Time of the first peak

Fig. 2 Sample Data from IAW Experiment ($P_{chamber}$ = 1.0 mTorr, I_{dis} = 30 mA, and V_{bat} = 0 V)

IV. Single-species Plasma Experiments

Single-species plasma experiments were conducted in the White Vacuum Chamber. The plasma was generated using argon at varied $P_{chamber}$, I_{dis}, and V_p while keeping V_{dis} constant. Steady-state properties of these plasmas were characterized by electrostatic probe measurements (EmP and LmP). Dynamic responses of the plasma perturbed by the pulsed voltage application were investigated by the WL and the WC setup. In the wave experiments, we varied the applied pulse shape (up and down), V_{bat}, and $P_{chamber}$ to characterize the WL and the WC setup.

A. Probe Measurement Results

Figure 3a and Figure 3b shows the electron temperatures and the electron deisities obtained by the LmP vs. I_{dis} for three $P_{chamber}$; 0.1, 0.5, and 1.0 mTorr. The case with V_p = +10 V was not included in Fig. 3. It is assumed that the size of error for I_{dis} = ± 1 mA. As shown in Figs. 3a and 3b, the plasma properties at $P_{chamber}$ = 0.5 and 1.0 mTorr were close. Assuming neutral particles follow an ideal gas law, there was only a two-fold difference in the neutral densities and thus in electron-neutral mean free paths. Such a difference had a small impact on altering the properties of the plasma in the MPC.

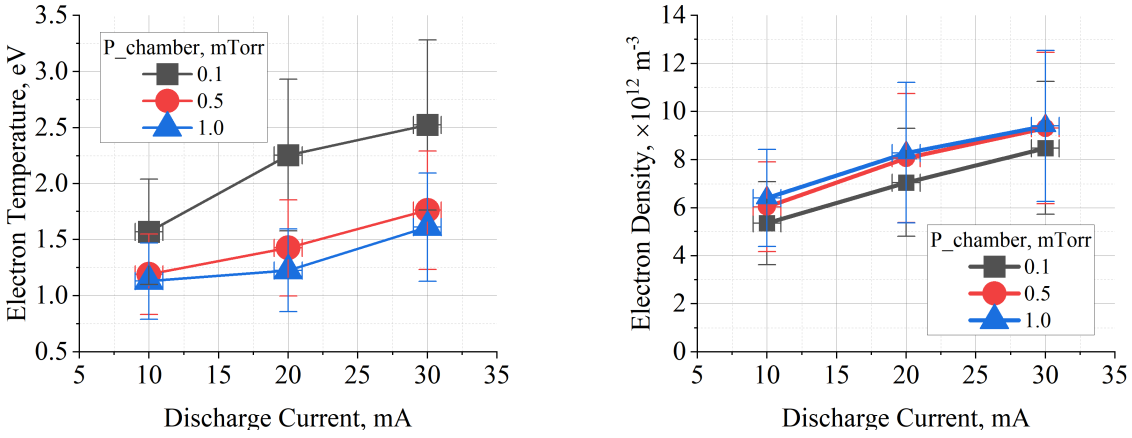

(a) Electron Temperature vs. Discharge Current **(b) Electron density vs. Discharge Current**

Fig. 3 Plasma Properties obtained by the Lmp for different Chamber Pressures (V_p = -10 V)

Table 1 summarizes the plasma properties at I_{dis} = 30 mA.

Table 1 Steady-state argon plasma properties from probe diagnostic at I_{dis} = 30 mA

Chamber Pressure, mTorr	0.1	0.5	0.5	1.0
Plasma Potential, V	-10.6±1.0	-9.6±1.0	+10.0±1.0	-9.4±1.0
Electron Temperature, eV	2.5±0.2	1.8±0.2	1.4±0.1	1.6±0.1
Electron Density, $\times 10^{12}$ m^{-3}	8.5±2.8	9.3±3.1	9.5±2.8	9.4±3.1
Debye Length, $\times 10^{-3}$ m	4.1±0.7	3.2±0.6	2.9±0.5	3.1±0.6

B. IAW Experiment Results

In the IAW Experiments, the plasma was generated at the fixed I_{dis} and V_{dis}, 30 mA and -60 V, respectively. In order to characterize and validate the WL and the WC setup, we varied the shape of the pulse applied to the WL, the biasing voltage on the WC, and the background chamber pressure.

1. Comparison of different applied pulses

First, we characterized the WL by changing the shape of applied signals. Figure 4 compares two different shapes of the signals applied to the WL. The up pulse shape shown in Fig. 4a means the pulse was applied from -10 V to +10 V, which looks like "⊥." On the other hand, the down pulse shape shown in Fig. 4b means the pulse was applied from +10 V to -10 V, which looks like "T." Both shapes repeated the 100 μs pulses every 10 ms (1% duty cycle). The plasma was generated at $P_{chamber}$ = 0.5 mTorr. In order to minimize the sheath formed around the WL before the pulse applications, the plasma potential was adjusted to the pre-pulse potential of each shape. V_p was adjusted to -10 V when the up pulses were applied and +10 V when the down pulses were applied. As shown in Fig.4, the applied signals were independent of Z_{LC} for both shapes. It confirms that the WL perturbed the plasma in the same way in every Z_{LC}, regardless of the applied voltage shapes.

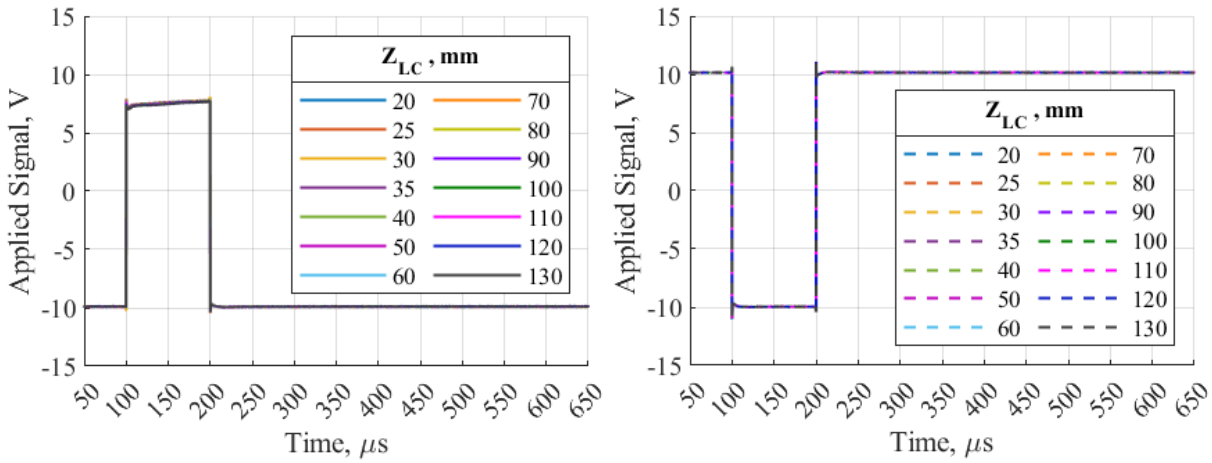

(a) Up (⊥) Pulses **(b) Down (T) Pulses**

Fig. 4 Applied Pulses vs. Time for Up (⊥) and Down (T) pulses ($P_{chamber}$ = 0.5 mTorr, I_{dis} = 30 mA, and V_{bat} = -45 V)

Figure 5 shows the signals collected by the WC at different Z_{LC} for the up and down pulses shown in Fig. 4. The solid lines and circle markers represent the collected signals and the peak from up (⊥) pulses. The dashed lines and triangle markers represent the collected signals and the peak from down (T) pulses. The black solid and red dashed vertical lines represent the peak searching domains for the up and down shapes, respectively (110 and 195 μs for the up pulses and 220 and 270 μs for the down pulses). It was found that the formation of IAW was observed more clearly when the WL's potential went down. In other words, the IAW was generated with a negative sheath formation which repels electrons near the WL.

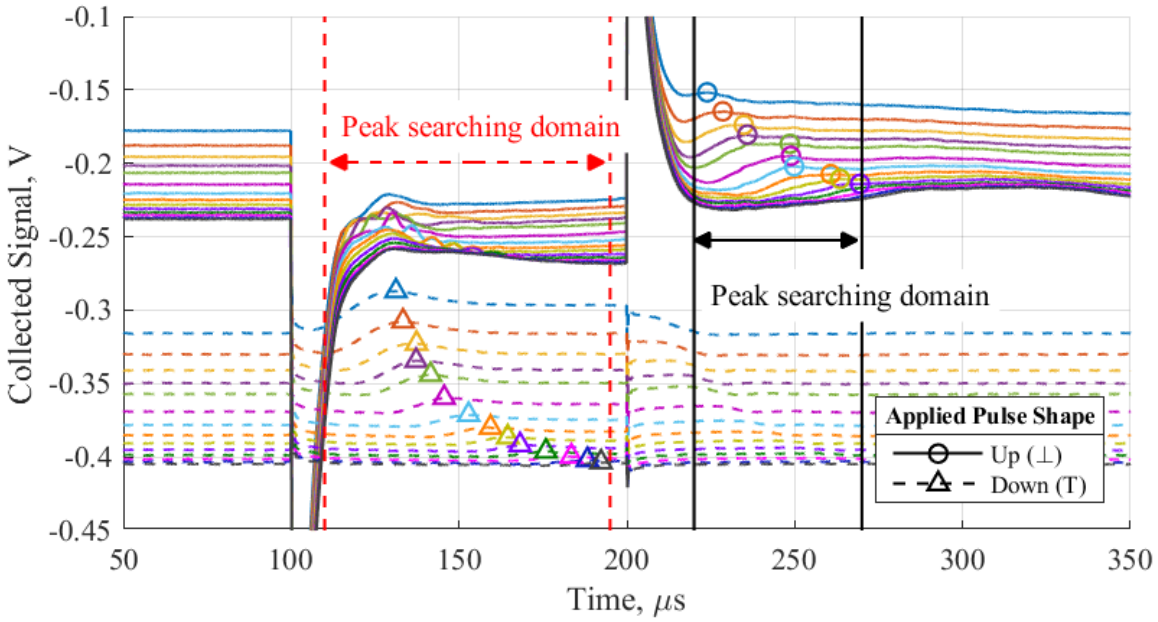

Fig. 5 Collected Signals vs Time for Up (⊥) and Down (T) pulses ($P_{chamber}$ = 0.5 mTorr, I_{dis} = 30 mA, and V_{bat} = -45 V)

Figure 6 shows Z_{LC}'s vs. the arrival time of the first peaks shown in Fig. 5. The black dot line represents the linear fitted curve for the up pulses, and the red dashed line represents the one for the down pulses. The peaks obtained when $Z_{LC} \geq 100$ mm for the up pulse shapes were not included in Fig. 6, and not used for the linear fit. The signals

collected at these distances were weak enough that no clear peak was found. The phase speed of the IAW generated by the up pulses was approximately 1530 m/s, and the one by the down pulses was approximately 1740 m/s. With the error size calculated in Sec. III.D, these two speeds of the IAW generated by different pulsed voltages agree with each other. Therefore, it is concluded that the formation of the IAW does not strongly depend on the shape of the pulsed voltage applied to the WL. In the following IAW experiments, the up pulse shape will be chosen to observe the plasma's responses after the pulse application with a longer time frame. The up pulse shape was used previously to generate the IAW in the MPC setup [17, 21].

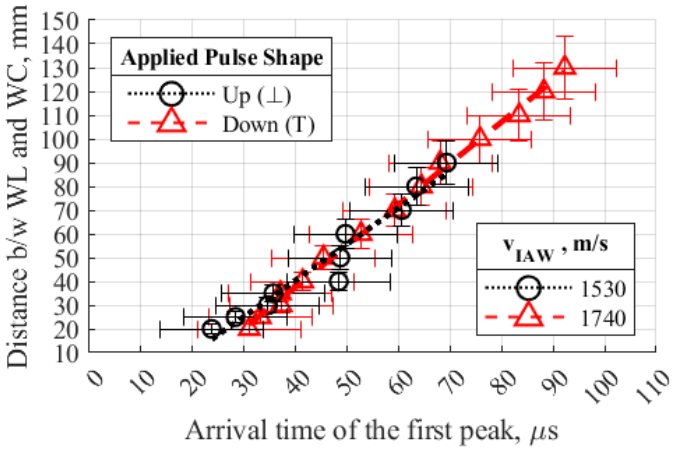

Fig. 6 Distance between WL and WV vs. Arrival Time of the first peak for Up (⊥) and Down (T) pulses ($P_{chamber}$ = 0.5 mTorr, I_{dis} = 30 mA, and V_{bat} = -45 V)

2. Comparison of different 45-V biasing battery units

Second, we changed the biasing voltage on the WC to characterize the WC and the detection circuit. The plasma was generated at $P_{chamber}$ of 0.5 mTorr, I_{dis} of 30 mA, and V_p of -10 V. Three WC biasing voltages were tested; V_{bat} = -45, ±0, and +45 V. V_{bat} = -45 V means that the negative side of the 45-V biasing battery unit was connected to the WC, and V_{bat} = +45 V means the positive side was connected to the WC. V_{bat} = ±0 V means the 45-V biasing battery unit was taken out from the detection circuit. The same peak searching domain between 220μs and 270μs was used for all three cases. Figs. 7a, 7b, and 7c show the signals collected by the WC at different Z_{LC} for V_{bat} = +45 V, -45 V, and ±0 V, respectively. As shown in Fig. 7, there is a difference in the magnitude of the collected signal during unperturbed periods. Furthermore, the negative signals were collected only when V_{bat} = -45 V. It indicates that the 45-V WC biasing voltage unit successfully selected the type of charged particles collected by the WC. When V_{bat} = -45 V, it is considered that the WC repelled most of the electrons, and the collected signals were mainly due to ions. On the other hand, when V_{bat} = -45 V, it is considered that the WC repelled most of the ions, and the collected signals were mainly due to electrons. When V_{bat} = ± 0V, it is assumed that the WC collected both electrons and ions, but the lighter electrons contribute to the amplitude of the collected signals as shown in Figs. 7a and 7b. It results in the higher amplitudes of the collected signals at V_{bat} = +45 V compared to the ones at V_{bat} = ±0 V.

Figure 8 shows Z_{LC}'s vs. the arrival time of the first peaks shown in Fig. 7. The black dotted, red dashed, and blue dash-dotted lines are the linear fitted curve for V_{bat} = -45, ±0, and +45 V cases, respectively. The peaks obtained when $Z_{LC} \geq$ 100 mm for all three cases were not included in Fig. 8, and not used for the linear fit. The phase speeds of the IAW were approximately 1530, 1680, and 1710 m/s for V_{bat} of -45, ±0, and +45 V respectively. With the error size calculated in Sec. III.D, these three speeds of the IAW obtained by the collection of the different charged particles agree with each other. Therefore, it is concluded that the WC setup successfully captured the IAWs, which are driven by ion and electron motions at the same speed. In the following IAW experiments, no 45-V WC biasing voltage will be used (V_{bar} = ±0 V). As shown in Fig. 7, it was found the ratio of the peak amplitude to the steady-state amplitude (= $A_{peak}/A_{steady\text{-}state}$) was larger as V_{bat} went more negative (approximately 14.7%, 9.6%, and 7.2% for V_{bat} of -45, ±0, and +45 V, respectively). However, the peaks appeared sharply and became more easily obtained with more positive V_{bat}. V_{bat} = ±0 V is the intermediate between these two limits, making it relatively easy to find the peak. It is considered that the collection of the IAW at this potential can capture the most natural state of it because it collects both electrons and ions.

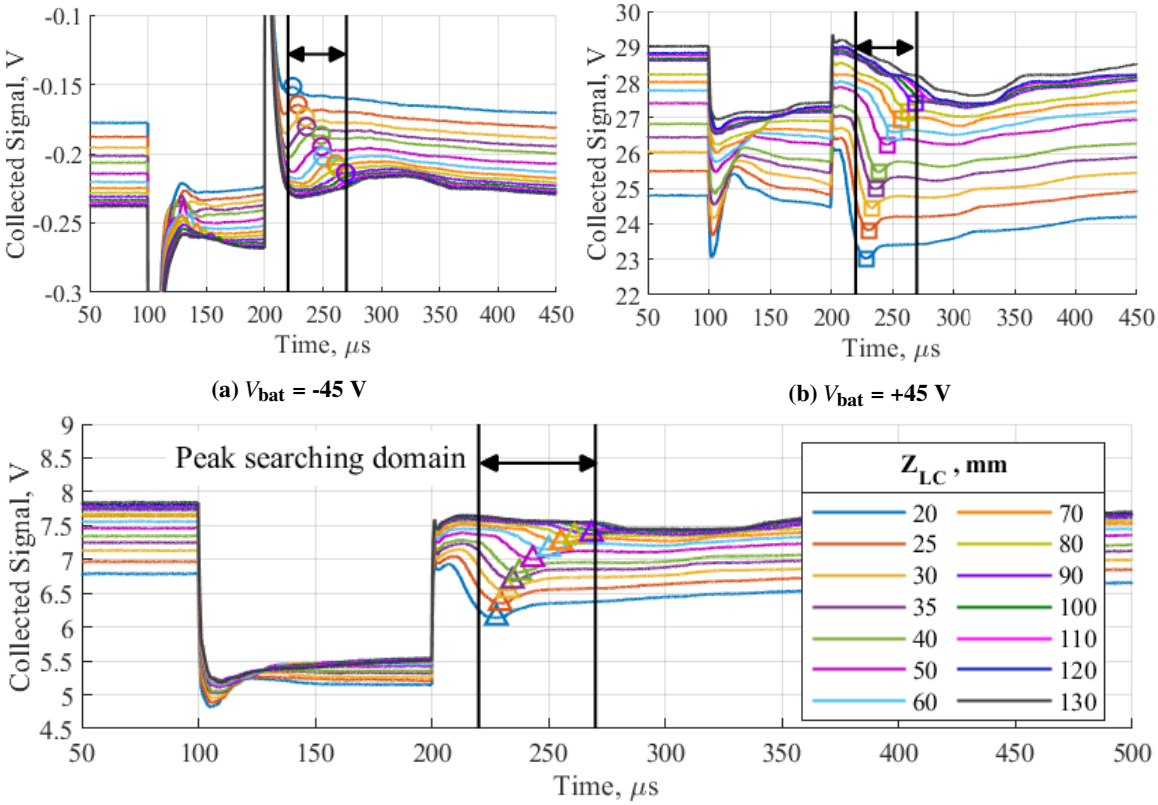

(a) V_{bat} = -45 V

(b) V_{bat} = +45 V

(c) V_{bat} = ±0 V (no 45-V biasing battery unit was used)

Fig. 7 Collected Signals vs. Time for different 45-V WC Biasing Battery Units ($P_{chamber}$ = 0.5 mTorr, I_{dis} = 30 mA, and V_p = -10 V.)

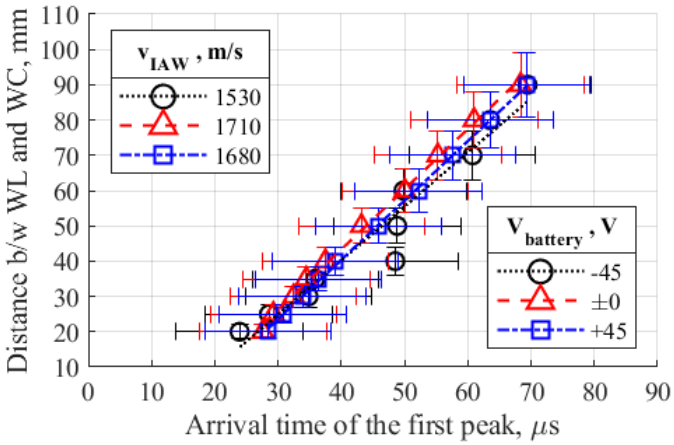

Fig. 8 Distance between WL and WC vs Arrival Time of the first peak for different 45-V WC Biasing Battery Units ($P_{chamber}$ = 0.5 mTorr, I_{dis} = 30 mA, and V_p = -10 V)

3. Comparison of different chamber pressures

Finally, we varied the chamber pressures to change the property of the plasma where the IAW was generated. The plasma was generated at the fixed I_{dis} = 30 mA and V_p = -10 V, but at three different $P_{chamber}$: 0.1, 0.5, and 1.0 mTorr. The steady-state plasma parameters were determined by the LmP and they are summarized in Table 1. Figure 9 shows Z_{LC} vs. the arrival time of the first peaks for each collected signal at different Z_{LC}. The black dotted, red dashed, and

blue dash-dotted lines are the linear fitted curve for P_{chamber} = 0.1, 0.5, and 1.0 mTorr cases, respectively. The peaks obtained when $Z_{\text{LC}} \geq 100$ mm for $P_{\text{chamber}} \geq 0.5$ mTorr were not included in Fig. 9, and not used for the linear fit. The phase speeds of the IAW were approximately 1890, 1710, and 16300 m/s for P_{chamber} of 0.1, 0.5, and 1.0 mTorr, respectively. With the Eq. 1, the electron temperatures corresponding to the measured phase speeds were 1.5, 1.2, and 1.1 eV, respectively. Based on the error propagation theory, the estimated error in the electron temperature from the wave experiment is approximately 30%. Compared to the electrostatic probe measurements, the electron temperatures obtained by the LmP and from the wave experiments agree with each other with approximately 40% error maximum.

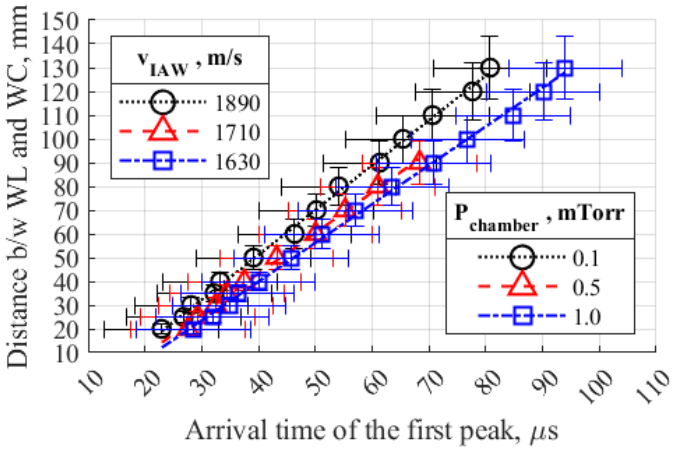

Fig. 9 Distance between WL and WC vs. Arrival Time of the first peak for different Chamber Pressures (I_{dis} = 30 mA, V_p = -10 V, and V_{bat} = ±0 V)

V. Computational Work

We performed the steady-state Particle-in-Cell (PIC) simulations for the devices used in the experiments with multiple species plasma. The simulations were performed in a 2D domain of size 100 × 100 mm, shown in Fig. 10a, with the plasma density of 1.0×10^{13} m^{-3} in the domain. We had previously performed simulations with single species to study how the plasma system behaves when an electron-scale pulse is applied to the system[31]. In a similar setup, we apply a constant -100 V to the pulse plate and let the system evolve with two ion species in the domain. In Fig. 10b, we show a preliminary result for argon and xenon two-species plasma where the top and bottom halves show argon and xenon bulk velocities, respectively. The blue line in Fig. 10b is the kinetic sheath edge, and the solid black lines are the sheath edges based on the Bohm sheath criteria. While both species seem to show a similar sheath thickness based on the Bohm sheath criteria, it should be noted that further analysis needs to be performed on these results to verify that this state does not change with time. Also, further investigation is required to assess the effect of background electron temperature (and therefore the ion acoustic speeds) on the sheath structure. Finally, in future work, we will apply a pulse to such a steady-state system to understand its effect on the sheath edge velocities.

VI. Conclusion

In this study, we generated a steady-state single-species argon plasma in the MPC with the hot filament discharge. The steady-state plasma parameters were determined by the EmP and the LmP. The fast pulsed voltage was applied to the plasma to generate the IAW, and the phase speed of the IAW was measured by collecting the signals at multiple locations.

We found that the IAW was generated when the wave launcher's potential went down. In the range of ±10 V from the plasma potential, the potential drop generated the IAW, regardless of whether the WL's potential was higher or lower than the plasma potential. When the wave launcher's potential went up, the perturbation of the plasma was small, and no apparent wave formation could be confirmed. We also found that the phase speed of the generated IAW wave was independent of the distance between the WL and the WC, the applied pulse shape (direction), and the WC's biasing potential. Furthermore, when the electron temperature was different at different chamber pressures, the phase speed of the IAW was varied. The electron temperatures corresponding to the measured phase speeds agreed with the electron

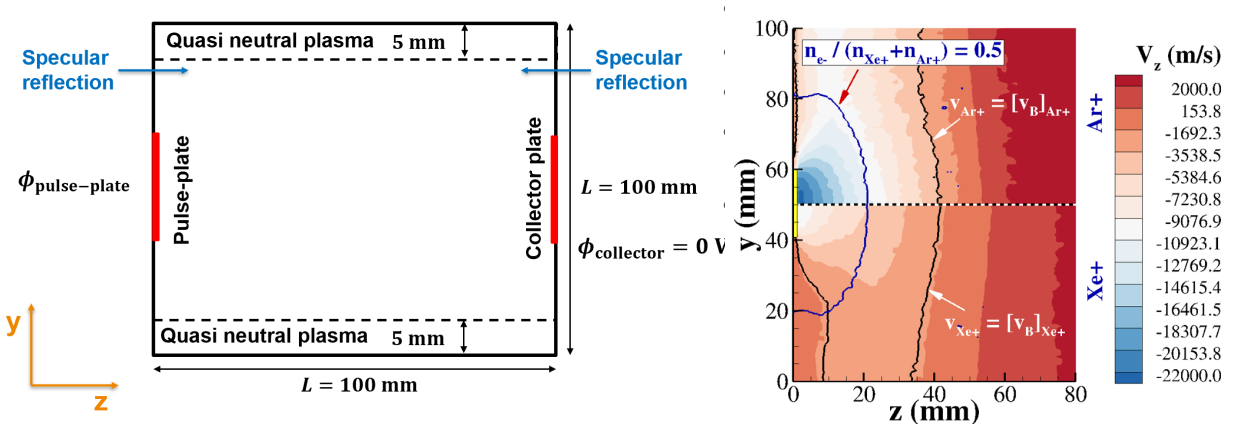

(a) Computational domain

(b) Bulk velocity of Ar^+ Xe^+ ion species.

Fig. 10 (a) Computational domain with $\phi_{pulse-plate} = -100$ V. (b) A comparison of bulk velocity of ions with sheath edges defined based on number density (blue line) and Bohm sheath criteria.

temperature obtained by the LmP with approximately 40% error maximum.

In future work, we will generate a noble-gas multi-species plasma in the same MPC. The relative ion concentration will be determined with the Eq. 3. Based on the error propagation theory, the error in the ion concentration is the same as the error in the electron temperature. Therefore, the error of 30-40% in the ion concentration is expected with our setup. A PIC simulation will be developed for multi-species plasma, and the dynamic evolution of the sheath around the WL and the IAW will be studied. Then the multi-species plasma will be generated from molecular-based gases, and the dynamic plasma behavior and the sheath physics of the low-density and multi-species plasma will be studied. Such an advanced understanding of sheath physics will be applied to developing a new diagnostic tool for EP plasma thrusters using molecular-based gas as their propellants. Also, understanding the sheath physics in the low-density multi-species plasma will potentially enable an optimized design to minimize plasma loss and thus improve performance.

Appendix

A. Electrostatic Probe Data Analysis Method

Figure 11 shows the EmP's measured I-V curve (solid blue line), the noise-reduced I-V curve (orange dot line)) made by the MATLAB® *ischange* function, and the inflection points obtained by the MATLAB® *ischange* function (green circles). EmP starts emitting electrons when the biasing voltage is lower than V_p because the emission is suppressed by the potential difference when the biasing voltage is higher than V_p. The MATLAB® *ischange* function was applied to the domain between -25 V and +5 V, which is shown as black dashed lines. The '*linear*' method was selected and the 'MaxNumChanges' was chosen to be 4. For the case in Fig. 11, V_p was determined to be approximately at -9.6 V. The expected error size is ±1.0 V for all EmP measurements.

Figure 12 shows the LmP's measured I-V curve (blue solid line), the IIEE(Ion Induced Electron Emission)-adjusted I-V curve (orange dash line), the linear-fitted ion-only I-V curve (green dot line), and the plasma potential (black solid line). With a constant γ of 0.096 [32, 33], the IIEE-adjusted I-V curve was approximated as

$$I_{\mathrm{LmP}} = \frac{I_{\mathrm{measured}}}{1+\gamma} \tag{5}$$

In the LmP's I-V curve, there is the ion-only region where the biasing voltage is negative enough to repel all electrons by the LmP. I_i was obtained by applying a linear-fit to I_{LmP} in the ion-only region, which was assumed to be between -150 V and -100 V. In a low-density plasma, n_e is often obtained from I_i using OML (Orbital Motion Limited) theory with the Bohm approximation, i.e., ions reach the Bohm speed at the sheath edge ($v_{i,s} = v_B = \sqrt{k_B T_e/m_i}$) [34]. However, the direct application of OML theory with the Bohm approximation was not used since we consider ions

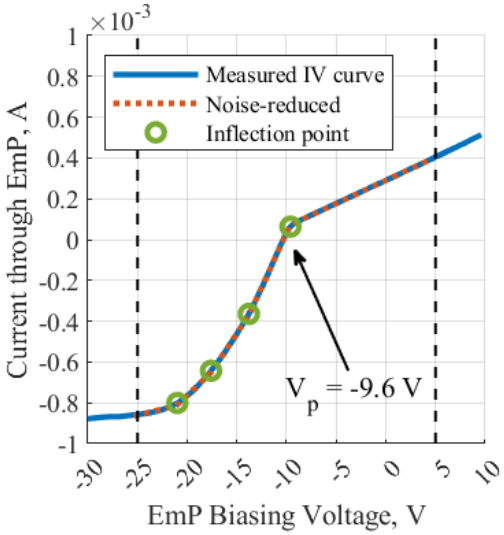

Fig. 11 Sample EmP's IV curve (when P_{chamber} = 0.5 mTorr, I_{dis} = 30 mA), and the 1.5V battery was used to bias the MPC)

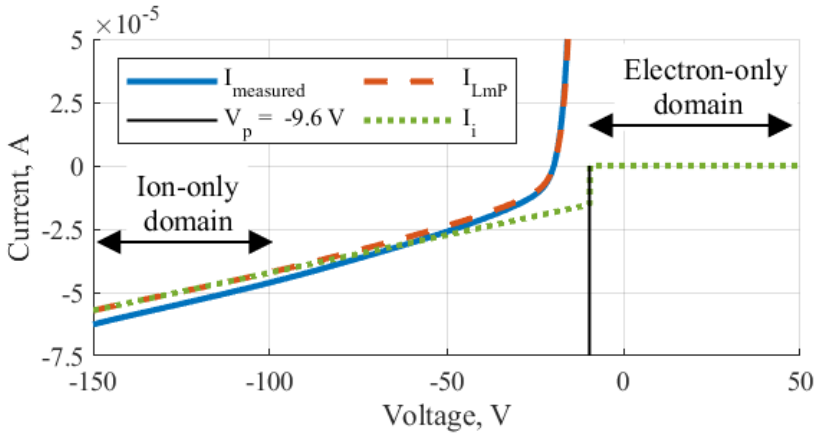

Fig. 12 Sample LmP's IV curve (when P_{chamber} = 0.5 mTorr, I_{dis} = 30 mA), and the 1.5V battery was used to bias the MPC)

did not actually reach the Bohm speed at the sheath edge in the plasmas formed in the experiments. In this work we estimate $T_{i,s}$ based on their measurements, and it is assumed to be 0.15±0.10 eV. Using OML theory and the assumed $T_{i,s}$, the linear-fitted I_i can be approximated as

$$I_i = \frac{1}{4} e n_{e,s} v_{i,s} A_c = \frac{1}{4} e \alpha n_e \sqrt{\frac{8 k_B T_{i,s}}{\pi m_i}} A_c \tag{6}$$

α needs to be defined based on the hot ion temperature model, and it was obtained by calculating Φ_{ps} required to accelerate ions to their hotter thermal speed. With the assumption of a Maxwellian distribution for electrons, α was approximated as

$$\alpha = \frac{n_{e,s}}{n_e} = \exp\left(-\frac{e\Phi_{ps}}{k_B T_e}\right) = \exp\left(-\frac{4T_{i,s}}{\pi T_e}\right) \tag{7}$$

For example, using Eq. 7, $\alpha = 0.826$ for $T_{i,s} = 0.15$ eV and $T_e = 1$ eV. A_c was obtained by calculating b with OML theory. b determines if an ion entering the sheath will hit (and be collected) by the LmP or not; when an ion enters the sheath with a distance of b or less, it will be collected by the LmP and vice versa. b was obtained by solving conservation of

ions' angular momentum and energy at the sheath edge and the LmP surface. Using the assumed $T_{i,s}$ and the hot ion temperature model, b was approximated as

$$b = r_{\mathrm{LmP}}\sqrt{1+\frac{\pi}{4}\frac{e(V_p - V_{\mathrm{probe}})}{k_B T_{i,s}}} \tag{8}$$

where V_{probe} is the LmP's biasing voltage. We assume A_c expands spherically, and A_c was approximated as

$$A_c = 4\pi b^2 \tag{9}$$

T_e was obtained by applying an linear fit to a natural log of I_e in the electron-only region. We assume that the plasma formed in the experiments followed the single-Maxwellian energy distribution function. We also assume that the population of the primary electrons is negligible because secondary (plasma) electrons are normally dominant in the MPC plasmas except near the wall (≥98% in the population [35]). I_e was approximated as

$$I_e = I_{\mathrm{LmP}} - I_i \tag{10}$$

In the electron-only domain, we take a linear fit to a natural log of I_e. The linear fit was applied to the fitting domain between the floating potential and the plasma potential. The linear fit was applied to give a steepest slope in the fitting domain, as shown in Fig. 13.

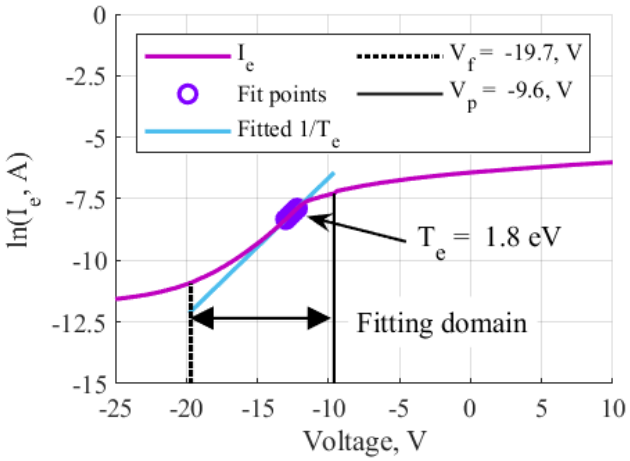

Fig. 13 Sample electron temperature curve fit (when P_{chamber} = 0.5 mTorr, I_{dis} = 30 mA), and the 1.5V battery was used to bias the MPC)

Acknowledgments

This work is supported by the AFOSR grant AF FA9550-19-1-0164, "Experiments, Modeling and Simulation of Advanced Materials-Plasma Interactions in the Space Environment". This work was also supported in part by the Department of Education through the Graduate Assistance in Areas of National Need Fellowship Program award P200A180050-19 at the Department of Aerospace Engineering, at the University of Illinois Urbana-Champaign.

References

[1] Rovey, J. L., Lyne, C. T., Mundahl, A. J., Rasmont, N., Glascock, M. S., Wainwright, M. J., and Berg, S. P., "Review of multimode space propulsion," *Progress in Aerospace Sciences*, Vol. 118, 2020, p. 100627. https://doi.org/10.1016/j.paerosci.2020.100627, URL https://linkinghub.elsevier.com/retrieve/pii/S0376042120300397.

[2] Berg, S. P., and Rovey, J. L., "Assessment of High-Power Electric Multi-Mode Spacecraft Propulsion Concepts," The George Washington University, 2013.

[3] Berg, S. P., and Rovey, J., "Assessment of Multi-Mode Spacecraft Micropropulsion Systems," *50th AIAA/ASME/SAE/ASEE Joint Propulsion Conference*, American Institute of Aeronautics and Astronautics, Cleveland, OH, 2014. https://doi.org/10.2514/6.2014-3758, URL http://arc.aiaa.org/doi/10.2514/6.2014-3758.

[4] Schonherr, T., Komurasaki, K., Romano, F., Massuti-Ballester, B., and Herdrich, G., "Analysis of Atmosphere-Breathing Electric Propulsion," *IEEE Transactions on Plasma Science*, Vol. 43, No. 1, 2015, pp. 287–294. https://doi.org/10.1109/TPS.2014.2364053, URL http://ieeexplore.ieee.org/document/6945885/.

[5] Singh, L. A., and Walker, M. L., "A review of research in low earth orbit propellant collection," *Progress in Aerospace Sciences*, Vol. 75, 2015, pp. 15–25. https://doi.org/10.1016/j.paerosci.2015.03.001, URL https://linkinghub.elsevier.com/retrieve/pii/S0376042115000226.

[6] Romano, F., "D4.1 - Literature Review of ABEP Systems," 2020, p. 23.

[7] Zheng, P., Wu, J., Zhang, Y., and Wu, B., "A Comprehensive Review of Atmosphere-Breathing Electric Propulsion Systems," *International Journal of Aerospace Engineering*, Vol. 2020, 2020, pp. 1–21. https://doi.org/10.1155/2020/8811847, URL https://www.hindawi.com/journals/ijae/2020/8811847/.

[8] Spektor, R., and Jones, K. L., "A BREATH OF FRESH AIR: AIR-SCOOPING ELECTRIC PROPULSION IN VERY LOW EARTH ORBIT," Tech. rep., 2021.

[9] Nakagawa, Y., Tomita, D., Koizumi, H., and Komurasaki, K., "Design and Test of a 100 N-class Thrust Stand for a Miniature Water Ion Thruster with CubeSat," *TRANSACTIONS OF THE JAPAN SOCIETY FOR AERONAUTICAL AND SPACE SCIENCES, AEROSPACE TECHNOLOGY JAPAN*, Vol. 16, No. 7, 2018, pp. 673–678. https://doi.org/10.2322/tastj.16.673, URL https://www.jstage.jst.go.jp/article/tastj/16/7/16_673/_article.

[10] Nakagawa, Y., Ataka, Y., Koizumi, H., and Komurasaki, K., "Miniature Water Ion Thruster; 1 km/s-class Delta-V for a 6U CubeSat," 2019, p. 6.

[11] Nakagawa, Y., Koizumi, H., Kawahara, H., and Komurasaki, K., "Performance characterization of a miniature microwave discharge ion thruster operated with water," *Acta Astronautica*, Vol. 157, 2019, pp. 294–299. https://doi.org/10.1016/j.actaastro.2018.12.031, URL https://linkinghub.elsevier.com/retrieve/pii/S0094576517317496.

[12] Nakagawa, Y., Koizumi, H., Naito, Y., and Komurasaki, K., "Water and xenon ECR ion thruster—comparison in global model and experiment," *Plasma Sources Science and Technology*, Vol. 29, No. 10, 2020, p. 105003. https://doi.org/10.1088/1361-6595/aba2ac, URL https://iopscience.iop.org/article/10.1088/1361-6595/aba2ac.

[13] Cifali, G., Misuri, T., Rossetti, P., Andrenucci, M., Valentian, D., Feili, D., and Lotz, B., "Experimental characterization of HET and RIT with atmospheric propellants," 2011. https://doi.org/IEPC-2011-224.

[14] Sheppard, A., and Little, J., "Performance Analysis of an Electron Cyclotron Resonance Thruster with Various Propellants," *AIAA Propulsion and Energy 2021 Forum*, American Institute of Aeronautics and Astronautics, VIRTUAL EVENT, 2021. https://doi.org/10.2514/6.2021-3375, URL https://arc.aiaa.org/doi/10.2514/6.2021-3375.

[15] Swanson, D. G., *Plasma waves*, 2nd ed., Series in plasma physics, Institute of Physics Pub, Bristol ; Philadelphia, 2003. OCLC: ocm52256959.

[16] Francis F. Chen, *Introduction to plasma physics and controlled fusion*, 3rd ed., Springer Science+Business Media, New York, NY, 2015.

[17] Hala, A. M., and Hershkowitz, N., "Ion acoustic wave velocity measurement of the concentration of two ion species in a multi-dipole plasma," *Review of Scientific Instruments*, Vol. 72, No. 5, 2001, pp. 2279–2281. https://doi.org/10.1063/1.1340021, URL http://aip.scitation.org/doi/10.1063/1.1340021.

[18] Wang, X., and Hershkowitz, N., "Experimental studies of the two-ion species flow in the plasma presheath," *Physics of Plasmas*, Vol. 13, No. 5, 2006, p. 053503. https://doi.org/10.1063/1.2193927, URL http://aip.scitation.org/doi/10.1063/1.2193927.

[19] Oksuz, L., Lee, D., and Hershkowitz, N., "Ion acoustic wave studies near the presheath/sheath boundary in a weakly collisional argon/xenon plasma," *Plasma Sources Science and Technology*, Vol. 17, No. 1, 2008, p. 015012. https://doi.org/10.1088/0963-0252/17/1/015012, URL https://iopscience.iop.org/article/10.1088/0963-0252/17/1/015012.

[20] Hershkowitz, N., and Ghim (Kim), Y.-C., "Probing plasmas with ion acoustic waves," *Plasma Sources Science and Technology*, Vol. 18, No. 1, 2009, p. 014018. https://doi.org/10.1088/0963-0252/18/1/014018, URL https://iopscience.iop.org/article/10.1088/0963-0252/18/1/014018.

[21] Kim, N.-K., Huh, S.-R., Roh, H.-J., Park, S., and Kim, G.-H., "How to determine the relative ion concentrations of multiple-ion-species plasmas generated in the multi-dipole filament source," *Journal of Physics D: Applied Physics*, Vol. 48, No. 22, 2015, p. 225201. https://doi.org/10.1088/0022-3727/48/22/225201, URL http://stacks.iop.org/0022-3727/48/i=22/a=225201?key=crossref.c7d14ab5957a43b6b51848d4e0993ad2.

[22] Szmytkowski, C., Maciag, K., and Karwasz, G., "Absolute electron-scattering total cross section measurements for noble gas atoms and diatomic molecules," *Physica Scripta*, Vol. 54, No. 3, 1996, pp. 271–280. https://doi.org/10.1088/0031-8949/54/3/006, URL https://iopscience.iop.org/article/10.1088/0031-8949/54/3/006.

[23] Raju, G., "Electron-atom collision cross sections in argon: an analysis and comments," *IEEE Transactions on Dielectrics and Electrical Insulation*, Vol. 11, No. 4, 2004, pp. 649–673. https://doi.org/10.1109/TDEI.2004.1324355, URL http://ieeexplore.ieee.org/document/1324355/.

[24] Hershkowitz, N., "Sheaths: More complicated than you think," *Physics of Plasmas*, Vol. 12, No. 5, 2005, p. 055502. https://doi.org/10.1063/1.1887189, URL http://aip.scitation.org/doi/10.1063/1.1887189.

[25] Oksuz, L., Khedr, M. A., and Hershkowitz, N., "Laser induced fluorescence of argon ions in a plasma presheath," *Physics of Plasmas*, Vol. 8, No. 5, 2001, pp. 1729–1733. https://doi.org/10.1063/1.1358312, URL http://aip.scitation.org/doi/10.1063/1.1358312.

[26] Oksuz, L., and Hershkowitz, N., "Plasma, presheath, collisional sheath and collisionless sheath potential profiles in weakly ionized, weakly collisional plasma," *Plasma Sources Science and Technology*, Vol. 14, No. 1, 2005, pp. 201–208. https://doi.org/10.1088/0963-0252/14/1/022, URL http://stacks.iop.org/0963-0252/14/i=1/a=022?key=crossref.acd7e6f892e1a78dce5eccf8ae4b4939.

[27] Hood, R., Baalrud, S. D., Merlino, R. L., and Skiff, F., "Laser-induced fluorescence measurements of ion fluctuations in electron and ion presheaths," *Physics of Plasmas*, Vol. 27, No. 5, 2020, p. 053509. https://doi.org/10.1063/1.5142014, URL http://aip.scitation.org/doi/10.1063/1.5142014.

[28] Langendorf, S., Walker, M. L., Rose, L., Keidar, M., and Brieda, L., "Study of the Plasma-Wall Interface – Measurement and Simulation of Sheath Potential Profiles," *49th AIAA/ASME/SAE/ASEE Joint Propulsion Conference*, American Institute of Aeronautics and Astronautics, San Jose, CA, 2013. https://doi.org/10.2514/6.2013-4128, URL http://arc.aiaa.org/doi/10.2514/6.2013-4128.

[29] Langendorf, S., and Walker, M., "Effect of secondary electron emission on the plasma sheath," *Physics of Plasmas*, Vol. 22, No. 3, 2015, p. 033515. https://doi.org/10.1063/1.4914854, URL http://aip.scitation.org/doi/10.1063/1.4914854.

[30] Leung, K., Samec, T., and Lamm, A., "Optimization of permanent magnet plasma confinement," *Physics Letters A*, Vol. 51, No. 8, 1975, pp. 490–492. https://doi.org/10.1016/0375-9601(75)90021-3, URL https://linkinghub.elsevier.com/retrieve/pii/0375960175900213.

[31] Yamauchi, T., Nuwal, N., Sharma, A., Levin, D. A., and Rovey, J. L., "High Resolution Modeling for Deeper Understanding of Plasma Dynamics," *AIAA Science and Technology Forum and Exposition, AIAA SciTech Forum 2021*, American Institute of Aeronautics and Astronautics Inc, AIAA, 2021, pp. 1–13.

[32] Lieberman, M. A., and Lichtenberg, A. J., *Principles of Plasma Discharges and Materials Processing*, John Wiley & Sons, Inc., Hoboken, NJ, USA, 2005. https://doi.org/10.1002/0471724254, URL http://doi.wiley.com/10.1002/0471724254.

[33] Konuma, M., *Film Deposition by Plasma Techniques*, 1st ed., Vol. 10, Springer-Verlag Berlin Heidelberg, 1992.

[34] Ruzic, D. N., *Electric probes for low temperature plasmas*, American Vacuum Society, New York City, 1994. URL http://www.worldcat.org/oclc/814170865.

[35] Baalrud, S. D., Lafleur, T., Fox, W., and Germaschewski, K., "Instability-enhanced friction in the presheath of two-ion-species plasmas," *Plasma Sources Science and Technology*, Vol. 24, No. 1, 2015, p. 015034. https://doi.org/10.1088/0963-0252/24/1/015034, URL https://iopscience.iop.org/article/10.1088/0963-0252/24/1/015034.